Journal of Power Sources 195 (2010) 1676–1687

Contents lists available at ScienceDirect

Journal of Power Sources

journal homepage: www.elsevier.com/locate/jpowsour

Exergetic analysis and optimization of a solar-powered reformed methanol fuel cell micro-powerplant

Nico Hotz[a,*], Raúl Zimmerman[b], Christian Weinmueller[c], Ming-Tsang Lee[a], Costas P. Grigoropoulos[a], Gary Rosengarten[b], Dimos Poulikakos[c]

[a] University of California at Berkeley, Department of Mechanical Engineering, Laser Thermal Laboratory, 6177 Etcheverry Hall, Berkeley, CA 94720-1740, USA
[b] School of Mechanical & Manufacturing Engineering, University of New South Wales, Sydney, NSW, Australia
[c] ETH Zurich, Department of Mechanical and Process Engineering, Laboratory of Thermodynamics in Emerging Technologies, ETH Zentrum, CH-8092 Zurich, Switzerland

ARTICLE INFO

Article history:
Received 24 August 2009
Received in revised form
15 September 2009
Accepted 30 September 2009
Available online 7 October 2009

Keywords:
Portable fuel cell system
Methanol reforming
Solar collector
Low-temperature fuel cell
Exergy
Exergetic efficiency

ABSTRACT

The present study proposes a combination of solar-powered components (two heaters, an evaporator, and a steam reformer) with a proton exchange membrane fuel cell to form a powerplant that converts methanol to electricity. The solar radiation heats up the mass flows of methanol–water mixture and air and sustains the endothermic methanol steam reformer at a sufficient reaction temperature (typically between 220 and 300 °C). In order to compare the different types of energy (thermal, chemical, and electrical), an exergetic analysis is applied to the entire system, considering only the useful part of energy that can be converted to work. The effect of the solar radiation intensity and of different operational and geometrical parameters like the total inlet flow rate of methanol–water mixture, the size of the fuel cell, and the cell voltage on the performance of the entire system is investigated. The total exergetic efficiency comparing the electrical power output with the exergy input in form of chemical and solar exergy reaches values of up to 35%, while the exergetic efficiency only accounting for the conversion of chemical fuel to electricity (and neglecting the 'cost-free' solar input) is increased up to 59%. At the same time, an electrical power density per irradiated area of more than 920 W m^{-2} is obtained for a solar heat flux of 1000 W m^{-2}.

1. Introduction

Low-temperature fuel cells fed by hydrogen offer several advantages for generating electrical power, namely high energy and power densities per mass and volume, high energy conversion efficiencies, instantaneous recharging, and fast response to load changes. The most popular type of fuel cell is the proton exchange membrane (PEM) fuel cell, which is already commercially available and can be operated with a hydrogen feed at temperatures typically between 60 and 90 °C. However, due to the low energy density of hydrogen per volume, the storage of hydrogen within a small fuel cell system is not only difficult and potentially dangerous, but as well very cumbersome and bulky. Therefore, a common solution is to store liquid hydrocarbon [1–7] or alcoholic fuels [8–14] and convert them to a hydrogen-rich reformate gas that can be subsequently used in a fuel cell.

Due to its reasonable energy density, very simple storage, easy worldwide availability and potential production from renewable sources, methanol is a highly appropriate fuel for a fuel cell system in combination with a steam reformer [15]. Methanol steam reforming on a Cu-based catalyst can be performed with a high efficiency resulting in a reformate gas containing up to 75% hydrogen. Since steam reforming of methanol is endothermic, the reactor has to be externally heated to reach and maintain the necessary reaction temperature. Such reformed methanol fuel cell (RMFC) systems are seen to have potential advantages compared to simpler direct methanol fuel cells (DMFC) due to their higher overall efficiency [15].

A promising new idea is to combine the methanol steam reforming-fuel cell system with a solar thermal collector providing the required heat to the system in the form of cost-free, emission-free, and sustainable solar sunlight [16,17]. The main idea of this work is to show how the efficiency of such a solar-powered fuel cell micro-powerplant fed by methanol can be dramatically increased if solar energy is used as a heat source instead of other external heaters, e.g. fuel consuming burners.

In recent years, the idea of analyzing a fuel cell-based energy conversion system by means of an exergy analysis has become popular [15,18–22]. In particular when dealing with a solar-powered fuel cell system, an energetic analysis simply based on the first law of thermodynamics neglects a major point: a fair comparison and evaluation is needed for different qualities of energy, namely

* Corresponding author. Tel.: +1 510 642 1006; fax: +1 510 642 6163.
E-mail address: hotz@berkeley.edu (N. Hotz).

0378-7753/$ – see front matter © 2009 Elsevier B.V. All rights reserved.
doi:10.1016/j.jpowsour.2009.09.055

Nomenclature

a, b	coefficient for excess Gibbs free energy
a_i	(flow) availability of species i (W)
A, B	coefficient for reaction rate constants (mol kg^{-1} s^{-1})
c	coefficient for enthalpy
d	height (across flow direction) (m)
E	cell voltage (V)
E^0	Nernst potential (V)
$E_{R/D}$	activation energy (J mol^{-1})
F	Faraday constant (=96,485 C mol^{-1})
g^E	excess Gibbs free energy (J mol^{-1})
$G_{12/21}$	coefficient for excess Gibbs free energy
h	enthalpy of flow (W)
i	current density (A m^{-2})
I_{solar}	solar irradiance (W m^{-2})
k	reaction rate constants (mol m^{-3} s^{-1}) or (mol kg^{-1} s^{-1})
L	length (in flow direction) (m)
n	molar flow rate (mol s^{-1})
n_e	number of electrons
$n^d_{H_2O}$	osmotic drag coefficient
p	pressure (Pa)
p_i	partial pressure of species i (Pa)
P	electrical power (W)
R	universal gas constant (=8.3145 J mol^{-1} K^{-1})
s	entropy of flow (W K^{-1})
T	temperature (K)
U	hydrogen utilization
x	flow direction (m)
x_i	mole fraction of liquid phase i
X_i	mole fraction of gas phase i
Y_i	mass fraction of species i

Greek letters

α_{II}	absorbance of absorber coating
α_{conv}	convective heat transfer coefficient (W m^{-2} K^{-1})
$\alpha_{O_2/CO}$	coefficient for reaction rate constant
α_{ct}	charge transfer coefficient
β	coefficient for excess Gibbs free energy
ε	porosity
ε_{I-V}	emittance
η_{ref}	reforming efficiency
η_s	surface overpotential (V)
λ	air-to-fuel ratio
λ_{ins}	thermal conductivity of insulation (W m^{-1} K^{-1})
μ	exergetic efficiency only accounting for the chemical exergy input
μ_{tot}	total exergetic efficiency
ρ_I	reflectance of glass layer
ρ_{cat}	catalyst density (kg m^{-3})
τ	tortuosity
τ_I	transmittance of glass layer
$\tau_{12/21}$	coefficient for excess Gibbs free energy
φ_{ref}	molar water–methanol ratio at inlet
$\Delta\Phi$	membrane phase potential (V)
Ω	overall effectiveness factor

Subscripts

0	standard state (=298 K, 101 kPa)
1	methanol
2	water
a	anode side of fuel cell
c	cathode side of fuel cell
D	decomposition reaction
g	gas phase
ins	silica aerogel insulation
l	liquid phase
PEM	PEM fuel cell
PROX	PROX reactor
R	reforming reaction
ref	steam reformer

Superscripts

$'$	per width (m^{-1})
$''$	per area (m^{-2})
E	excess properties

solar irradiance, chemical energy stored in fuels, heat, and finally, electrical energy. These different forms of energy provide different availabilities to be converted to useful work or, in other words, they comprise different exergy contents. A thorough exergetic analysis is the only way to adequately compare thermal, chemical, and electrical energy.

The purpose of this work is to analyze and optimize a small, portable solar-powered RMFC system including a methanol steam reformer in the sense of exergetic efficiency. The effect of the main geometrical and operational parameters on the performance and efficiency of the entire micro-powerplant is investigated as well as the influence of the intensity of solar radiation.

2. System

The system has three inlet flows: a liquid methanol–water mixture from a reservoir, a small amount of air for the preferential oxidation (PROX) reaction, and a larger air flow to the cathode of the fuel cell (Fig. 1). In the evaporator, the initially liquid methanol–water mixture (1:1 molar mixing ratio) is heated up to the reformer temperature, where most of the heating power is required to evaporate the mixture. The necessary length of the evaporator/pre-heater depends on the desired reformer temperature and the flow rates of the inlet mixture. In the steam reformer, the methanol–water mixture is converted in the presence of a catalyst to H_2 and CO_2 at temperatures typically in the range of 220–300 °C. CO is obtained as a by-product through undesired methanol decomposition. The reformer can be operated to achieve high or even complete conversion of methanol and water, but the reformate gas may contain some remaining gaseous methanol and water. The reformate gas is then mixed with a small amount of ambient air and cooled down to the operating temperature of the PROX reactor (T_{PROX} = 353 K), where the mole fraction of CO is reduced below a critical mole fraction ($X_{CO,crit}$ = 10 ppm). The excess O_2 in the PROX reactor oxidizes some of the H_2, therefore slightly reducing the available fuel for the PEM fuel cell. The PROX product gas mixture is fed to the anode of the fuel cell, whereas the cathode is fed by air pre-heated to the PEM operating temperature in a second pre-heater. The anode and cathode outlet gases are mixed together and released to the ambient as exhaust gas, possibly containing traces of not reacted methanol, H_2, CO, and O_2 as well as larger amounts of water vapor, CO_2, and N_2. Potentially desirable post-treatment of the exhaust gas to remove toxic and flammable species is neglected herein. All three inlet flows, the air flow to the PROX reactor and to the PEM fuel cell, as well as the methanol–water mixture are assumed to be at ambient temperature (298 K) at the inlets.

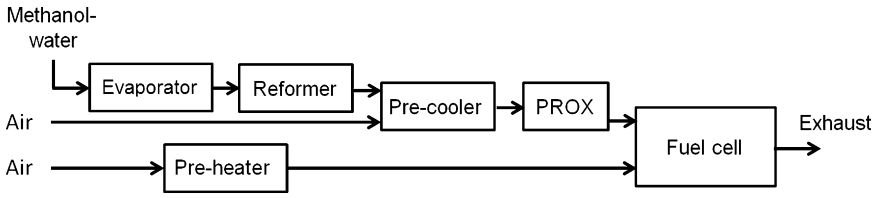

Fig. 1. Schematic of the mass flows in the system.

2.1. Thermal model

The entire system consists of three modules with specific thermal properties: a solar module (heated by solar radiation and vacuum-insulated), an intermediate module (no solar radiation and no insulation), and the fuel cell module (no solar radiation and silica aerogel insulation).

The solar module (Fig. 2a) contains the steam reformer and the pre-heaters for the methanol–water mixture as well as for the air flow to the fuel cell. These three components have in common that they have to be heated externally, which is achieved in our case by solar radiation. The top glass layer (I) has a reflectance $\rho_I = 0.08$, a transmittance $\tau_I = 0.92$, an emittance $\varepsilon_I = 0.84$, and a thickness of 2 mm. The surface of the top inner silicon layer (II) is coated with a selective coating (with an emittance $\varepsilon_{II} = 3.6 \times 10^{-7} T^2 - 1.48 \times 10^{-4} T + 0.036$ as a function of the surface temperature T in Kelvin and $\alpha_{II} = 0.95$), while the surfaces of the bottom vacuum layer (III and IV) have a highly reflective coating with a very low emittance ($\varepsilon_{III/IV} = 0.02$) to reduce radiative heat losses. The bottom surface (V) has a low emittance of $\varepsilon_V = 0.2$. The silicon layers of all three modules are 0.5 mm thick and the fluid channels are 0.1 mm deep. The details of this vacuum-insulated system are presented in [17]. A convective heat transfer coefficient $\alpha_{conv} = 10\ W\ m^{-2}\ K^{-1}$ is assumed for all surfaces in contact with the ambient.

The intermediate module (Fig. 2b) is used to prepare the H_2-rich reformate gas mixture for the fuel cell: first, it has to be cooled from the high reformer temperature (typically up to 600 K) to the lower fuel cell (and PROX) temperature. Secondly, the CO mole fraction in the reformate after methanol steam reforming is typically of the order of 1%, which is significantly high for a PEM cell, and has to be reduced e.g. by preferential oxidation of CO. This oxidation reaction is exothermic and therefore heat has to be removed from the PROX reactor as well as from the pre-cooler. To achieve this heat transfer, the fluid channel is not insulated and directly in contact with the ambient air. Convection and to some degree thermal radiation cool the fluid channels. The outer surfaces have an emittance of $\varepsilon_{I/V} = 0.9$.

The PEM fuel cell itself is the third module (see Fig. 2c). The thermal management of the fuel cell is essential: the electrochemical reactions in it are exothermic and heat has to be released from the fuel cell to the ambient to avoid overheating. On the other hand, the fuel cell temperature has to be kept at a certain level to achieve an efficient reaction of fuel and excessive heat transfer from the cell has to be avoided at the same time. In our case, the PEM module is insulated by a layer of silica aerogel (thermal conductivity $\lambda_{ins} = 13\ mW\ m^{-1}\ K^{-1}$ and a thickness of 12 mm) on both sides of the flow channel.

In all three modules, the following heat transfer mechanisms are taken into account: convective heat transfer between the fluid flow and the channel walls through forced convection, radiative heat transfer between different layers through the vacuum, conduction through the silica aerogel insulation as well as through all silicon

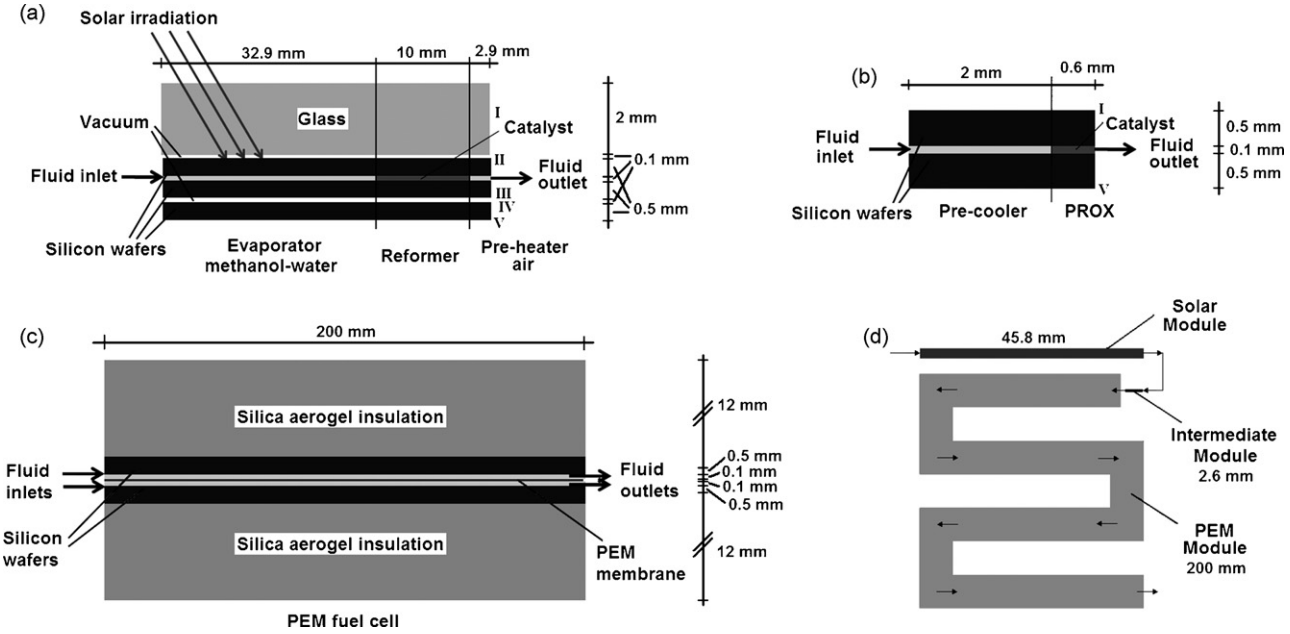

Fig. 2. (a) Schematic of solar module: the thickness of all layers is enlarged by the factor of 5 for better illustration. The lengths of the three components correspond to the reference case shown later. (b) Schematic of intermediate module: the lengths of the two components correspond to the reference case. (c) Schematic of PEM module: the thickness of the silica insulation is enlarged by the factor of 4, the other layers by the factor of 15 for better illustration. The length of the fuel cell corresponds to the reference case. (d) Schematic of the entire system with 4 turns for the reference case (not drawn to scale).

and glass layers, radiative and convective heat transfer (assuming a slow air stream over the modules) from the external walls to the ambient.

It is assumed that all three modules are perfectly insulated in the lateral direction and that no conductive heat transfer takes place between the three modules. Since the cross section of all layers (with thicknesses in the order of 10^{-3} m) is drastically smaller than the top and bottom area, the heat losses to the ambient in vertical direction are orders of magnitude larger than the heat transfer in horizontal direction.

To account for the flexibility and modularity of the design, all results are calculated per unit width, meaning that the lateral direction is not taken into account. Since the width in lateral direction is always several orders of magnitude larger than the height of the modules (again, with thicknesses of the order of 10^{-3} m), this assumption is always feasible. It is assumed that the solar module is placed on top of the entire system, with the intermediate and PEM module underneath, where the later is curved in a serpentine-like form to fit below the solar module (Fig. 2d). Depending on the length of the fuel cell, the serpentine consists of 1–7 turns for all results presented later (4 turns for the reference case of Section 3.1 and the results of 3.3, 1–7 turns for the Section 3.2, and 1–2 turns for Section 3.4). To ensure sufficient natural convection between the turns of the serpentine, the PEM module will have a thickness in the order of 3–4 cm, leading to a total system height of approximately 4–30 cm (below 18 cm for most cases). It is assumed that with this geometry the air temperature between the turns of the PEM module is the same as the surrounding ambient temperature. For the sake of simplicity of the numerical model, the possible usage of the waste heat released by all three modules for pre-heating of the inlet flows of air and methanol–water mixture is neglected. However, in a realistic application, the recycling of this excess heat will further increase the overall system efficiency significantly.

It is assumed that the temperature in each silicon or glass layer is constant. There are no temperature gradients along the length, width, or height of each wafer. This assumption, especially the critical assumption of constant temperature along the length of each silicon or glass layer, has been confirmed by 2-D calculations of entire modules (not shown in detail for brevity). It has been shown that the conductive heat transfer in these layers is several orders of magnitude higher than the heat transfer between the external layers and the ambient or between the inner layers and the fluid flow, etc. This is simply due to the high thermal conductivity of silicon and even glass and it is confirmed by the Biot numbers for the glass layer and the silicon layers, being in the order of 10^{-2} and 10^{-3}, respectively. It can be said that the conductive heat transfer within the silicon smoothes out any temperature variation immediately within these layers. Quantitative calculations showed temperature differences along the solar module of less than 0.3 K over a length of 2 cm even for extreme cases. Therefore, the temperature of all silicon and glass wafers has been assumed to be constant in the following calculations.

The temperature of the fluid flow varies markedly in the flow direction at the entrance of the modules and is almost constant after a short thermal entrance length. Temperature gradients in the fluid across the flow direction are neglected. The fluid temperature variation along the channels is slightly smoothed by conductive heat transfer in the fluid. Nevertheless, this conductive heat transfer is rather low compared to convective heat transfer (with thermal Peclet numbers significantly higher than unity) and especially when compared to the conductive heat transfer within the solid wafers, as described above, due to the low thermal conductivity of the fluids compared to the conductivity of the solid wafers (the thermal conductivities of glass and silicon are more than one and three orders of magnitude larger than that of the mass flow, respectively).

2.2. Reaction and phase change modeling

2.2.1. Evaporation of methanol–water mixture: non-random two-liquid theory (NRTL)

The vapor–liquid equilibrium of a methanol–water binary mixture is calculated by using the Antoine equation to compute the saturation vapor pressure and the NRTL model to estimate the activity coefficients and consider non-ideal mixing of the liquid phase. The non-random two-liquid model developed by Renon et al. [23–25] is used to calculate the excess enthalpy of the liquid phase. The original form of the NRTL model has the following form for the excess Gibbs free energy:

$$g^{\mathrm{E}} = R \cdot T \cdot x_1 \cdot x_2 \cdot \left[\tau_{21} \cdot \frac{G_{21}}{(x_1 + x_2 \cdot G_{21})} + \tau_{12} \cdot \frac{G_{12}}{(x_2 + x_1 \cdot G_{12})} \right], \quad (1)$$

where τ_{12} and τ_{21} are defined as $\tau_{12} = a_{12} + b_{12}/T$ and $\tau_{21} = a_{21} + b_{21}/T$; $G_{12} = \exp(-\beta \cdot \tau_{12})$ and $G_{21} = \exp(-\beta \cdot \tau_{21})$. The subscripts 1 and 2 denote the liquid components of methanol and water, respectively, and x is the mole fraction of the liquid species. The molar excess enthalpy h^{E}, which indicates the temperature dependence of the Gibbs free energy, can be determined using the Gibbs–Helmholtz relation:

$$\frac{h^{\mathrm{E}}}{R} = \frac{d(g^{\mathrm{E}}/(R \cdot T))}{d(1/T)}. \quad (2)$$

From the last two equations, the NRTL model for the molar excess enthalpy h^{E} leads to

$$h^{\mathrm{E}} = R \cdot x_1 \cdot x_2 \cdot \left(\frac{b_{21} \cdot G_{21} \cdot [x_1 \cdot (1 - \beta \cdot \tau_{21}) + x_2 \cdot G_{21}]}{(x_1 + x_2 \cdot G_{21})^2} + \frac{b_{12} \cdot G_{12} \cdot [x_2 \cdot (1 - \beta \cdot \tau_{12}) + x_1 \cdot G_{12}]}{(x_2 + x_1 \cdot G_{12})^2} \right). \quad (3)$$

The best fitting model was found in Horstmann et al. [26]. Using the parameters in Table 7 of Horstmann et al. [26], the parameters a_{12}, b_{12}, a_{21} and b_{21} are calculated and parameter β can be used directly:

$$a_{12} = -0.053179, \quad b_{12} = -110.35\,\mathrm{K}^{-1}, \quad a_{21} = 2.6953,$$
$$b_{21} = -414.65\,\mathrm{K}^{-1}, \quad \beta = 0.4700 \quad (3)$$

The molar enthalpy of a methanol–water vapor–liquid mixture is calculated relative to the enthalpy of pure methanol and pure water in the liquid phase at 298 K. For the liquid phase of the mixture, the excess enthalpy calculated by the NRTL method is included to account for the non-ideal mixing of methanol and water in the liquid phase. For the vapor phase, ideal gas mixing is assumed:

$$\Delta h_{\mathrm{tot}}(T) = h_{\mathrm{l,tot}}(T) + h_{\mathrm{g,tot}}(T) - h_{\mathrm{l},1}(T_0) - h_{\mathrm{l},2}(T_0)$$
$$= h_{\mathrm{l},1}(T) + h_{\mathrm{l},2}(T) + h^{\mathrm{E}}(T) + h_{\mathrm{g},1}(T) + h_{\mathrm{g},2}(T) - h_{\mathrm{l},1}(T_0) - h_{\mathrm{l},2}(T_0) \quad (4)$$

where 1 and 2 refer again to methanol and water, respectively. The molar enthalpies for liquid (l) and gas (g) phase are calculated using polynomial expressions:

$$h_i(T) = R \cdot T \cdot (c_1 + c_2 \cdot T + c_3 \cdot T^2 + c_4 \cdot T^3 + c_5 \cdot T^4) + c_6 \quad (5)$$

where the parameters c_i are taken from Moran and Shapiro [27] and the DIPPR Project 801 database [28]. The difference in total molar enthalpy between the start of evaporation (at 349.6 K) and complete evaporation (at 362.0 K) amounts to 38.48 kJ mol^{-1}.

2.2.2. Steam reforming of methanol

To quantitatively investigate the steam reforming of methanol, a reduced reaction model developed by Amphlett et al. [8] is

applied, assuming that the reaction is dominated by the reforming reaction

$$CH_3OH + H_2O \overset{k_R, k'_R}{\longleftrightarrow} CO_2 + 3H_2 \quad (6)$$

and the decomposition reaction

$$CH_3OH \xrightarrow{k_D} CO + 2H_2. \quad (7)$$

Using a simple reactive flow model by Lee et al. [10], the reaction rate constants read

$$k_R = (A_R + B_R \ln\varphi_{ref}) \exp\left[\frac{-E_R}{RT_{ref}}\right] \rho_{cat,ref} \quad (8)$$

for the reforming reaction and

$$k_D = A_D \exp\left[\frac{-E_D}{RT_{ref}}\right] \rho_{cat,ref} \quad (9)$$

for the decomposition reaction. The molar ratio of water and methanol is $\varphi_{ref} = 1$ for all results presented herein, R is the universal gas constant, and T_{ref} is the reformer temperature. The chosen steam-to-methanol ratio is relatively low and a higher φ_{ref} would improve the reforming reaction rate constant according to Eq. (8). Nevertheless, a higher water–methanol ratio would increase the total inlet flow rate, therefore significantly hampering the evaporation and pre-heating of the inlet flow. Since the length of the solar module and especially the evaporator length are crucial for the entire system performance, as it will be shown later, the molar ratio of water and methanol is kept at the stoichiometric value. The catalyst density in the packed bed $\rho_{cat,ref}$ and the kinetic parameters A_i, B_R, and E_i of the used $Cu/ZnO/Al_2O_3$ catalyst have previously been presented [15]:

$$\rho_{cat,ref} = 212\,\mathrm{kg\,m^{-3}}, \quad A_R = 5.75 \times 10^6\,\mathrm{mol\,kg^{-1}\,s^{-1}},$$
$$B_R = 4.705 \times 10^6\,\mathrm{mol\,kg^{-1}s^{-1}}, \quad E_R = 84.1\,\mathrm{kJ\,mol^{-1}},$$
$$A_D = 7.09 \times 10^7\,\mathrm{mol\,kg^{-1}s^{-1}}, \quad E_D = 111.2\,\mathrm{kJ\,mol^{-1}}.$$

2.2.3. Preferential oxidation of CO

A major drawback of using alcohol or hydrocarbon reformate as feed gas for PEM fuel cells is the inevitable high concentration of CO obtained as a by-product of the reaction. For steam reforming of methanol at temperatures above 200 °C, CO mole fractions in the order of one percent or more are expected, while the quantity increases for higher temperatures and longer reformer lengths. However, conventional PEM catalysts can only tolerate CO mole fractions below 10 ppm for long-term operation [29,30]. A straightforward solution to overcome this intrinsic problem of methanol reforming is the integration of a preferential oxidation reactor into the fuel cell system that oxidizes a large amount of the undesired CO in the reformate gas while reducing the precious H_2 only marginally. A small amount of air is mixed with the reformer outlet gas ($\lambda_{PROX} = 2 \cdot n'_{O_2,in}/n'_{CO,in} = 2$) and reacts over a $Au/\alpha\text{-}Fe_2O_3$ catalyst at 80 °C. The advantage of this catalyst is its high effectiveness and the convenient reaction temperature which is identical with the fuel cell inlet temperature, therefore decreasing the complexity of the thermal management. The amount of reacted CO and H_2 can be calculated by

$$\frac{dn'_{CO}}{dx} = k_{CO} \cdot p_{O_2}^{\alpha_{O_2}} \cdot p_{CO}^{\alpha_{CO}} \cdot \rho_{cat,PROX} \cdot d_{channel} \quad (10)$$

and

$$\frac{dn'_{H_2}}{dx} = k_{H_2} \cdot p_{O_2}^{\alpha_{O_2}} \cdot \rho_{cat,PROX} \cdot d_{channel}, \quad (11)$$

respectively, using data on the reaction kinetics from Kahlich et al. [31]:

$$k_{CO} = 0.981\,\mathrm{mol_{CO}\,kg_{Au}^{-1}\,s^{-1}}, \quad k_{H_2} = 0.481\,\mathrm{mol_{H_2}\,kg_{Au}^{-1}\,s^{-1}},$$
$$\alpha_{O_2} = 0.27, a_{CO} = 0.55, \quad \rho_{cat,PROX} = 34.5\,\mathrm{kg_{Au}\,m^{-3}}. \quad (11)$$

2.2.4. PEM fuel cell model

A fuel cell model has been developed and presented in [15], which is based on an analytical 1-D model by Gurau et al. [32]. The basic assumption of Gurau et al.'s model is that the performance of a H_2-fed PEM fuel cell is determined by reaction and diffusion processes on the cathode side. The fuel cell model can therefore be reduced to a 1-D half-cell of the cathode side including a cathode gas channel, a gas diffusion layer, a catalyst layer, and the fuel cell membrane [32]. The diffusion of O_2 across the half-cell is described by Fick's Second Law, considering the effective porosity ε, the tortuosity τ of the gas diffusion layer and the catalyst layer, and the consumption of O_2 by the fuel cell reaction in the catalyst layer. The cell voltage E

$$E = E^0 - \Delta\Phi - \eta_s \quad (12)$$

is a function of the cathode surface overpotential η_s, the membrane phase potential between anode and cathode $\Delta\Phi$, and the ideal reversible voltage or Nernst potential E^0. The current density of the fuel cell i can be defined as a function of the surface overpotential η_s

$$i = n_e F k \exp\left[\frac{\eta_s \alpha_{ct} n_e F}{RT}\right] d_{cl} \Omega Y_{O_2}, \quad (13)$$

where k is the reaction rate constant of the fuel cell reaction and d_{cl} is the thickness of the catalyst layer. The overall effectiveness factor Ω is given by [32]. By using the surface overpotential η_s as an independent parameter, the polarization curve can be described by Eqs. (12) and (13).

In this study, the 1-D model of Gurau et al. [32] is extended to a quasi-2-D PEM fuel cell model, similar to [15]. The 1-D model is used to describe the diffusion and reaction processes across the fuel cell. To consider the profiles of temperature and species concentrations along the anode and cathode channels, the channels are discretized. The variations of temperature and species concentrations lead to a non-uniform current density distribution along the fuel cell. Pressure losses in the channels are neglected and the cell voltage E is fixed as an operational parameter. It is assumed that there is no temperature difference between anode side, cathode side, and the membrane between them. Nevertheless, these temperatures vary along the flow direction depending on the chemical reactions and the heat transfer between the fluid flow and the surrounding silicon channel walls, which is a significant difference to the assumption of an isothermal cell [15]. The molar flow rates of H_2, water, and O_2 change along the fuel cell channels depending on the reaction rate, indicated by the current density i. The gradients in molar flow rate of H_2 in the anode channel and O_2 in the cathode channel read

$$\frac{dn'_{a,H_2}}{dx} = 2 \cdot \frac{dn'_{c,O_2}}{dx} = \frac{-i}{2F}, \quad (14)$$

whereas the gradient of molar water flow rate in the anode channel

$$\frac{dn'_{a,H_2O}}{dx} = \frac{-n^d_{H_2O} \cdot i}{F} \quad (15)$$

and the gradient of molar water flow rate in the cathode channel

$$\frac{dn'_{c,H_2O}}{dx} = \frac{(1/2 + n^d_{H_2O}) \cdot i}{F} \quad (16)$$

depend as well on the osmotic drag coefficient $n^{d}_{H_2O}$[33]. The gradient of generated electrical power per width dP' along the flow direction x for constant cell voltage E is written as

$$\frac{dP'}{dx} = iE, \tag{17}$$

where the current density i is calculated using Eq. (13). The total electric power generated by the fuel cell is obtained by integration of Eqs. (17) per the cell length L_{PEM}. For simplicity of the numerical code, the molar ratio of oxygen and hydrogen at the fuel cell inlets

$$\lambda_{PEM} = 2 \cdot \frac{n'_{O_2,in,PEM}}{n'_{H_2,out,\,ref}}. \tag{18}$$

is based on the hydrogen flow rate produced in the steam reformer. Since a small amount of H_2 is afterwards reacted in the PROX reactor, the effective air-to-fuel ratio in the fuel cell is slightly higher than the herein used λ_{PEM}. The following parameters of the PEM model are taken from [15]:

$k = 0.015\ \text{mol m}^{-3}\ \text{s}^{-1}$, charge transfer coefficient $\alpha_{ct} = 1.0$, thicknesses of gas channel $d_h = 1.0$ mm, of gas diffusion layer $d_{gdl} = 350\ \mu$m, of catalyst layer $d_{cl} = 10\ \mu$m, and of membrane $d_{mem} = 50\ \mu$m, effective porosity of the gas diffusion layer $\varepsilon_{gdl} = 0.7$ and of the catalyst layer $\varepsilon_{cl} = 0.2$, tortuosity of the gas diffusion layer $\tau_{gdl} = 1.5$ and of the catalyst layer $\tau_{cl} = 1.5$, volume fraction of ionomer of the catalyst layer $\varepsilon_{ion} = 0.136$, ionomer tortuosity of the catalyst layer $\tau_{ion} = 1.5$, Nernst potential $E^0 = 1.23$ V.

2.3. Numerical analysis of the system

The temperature and molar flow rate profiles of the fluid flows along the flow direction in all system components are derived by using a fourth-order Runge–Kutta method for steady state. Evaporation of the initially liquid methanol–water mixture and chemical reactions are included in the thermal and chemical model as source terms according to the previous subsection. The temperature of the silicon and glass layers is calculated for steady state using the thermal properties of conductive, convective, and radiative heat transfer presented in Section 2.1. The model of each system component is checked for grid independence and the finally used grid size has been chosen accordingly.

To calculate the performance and characteristics of the entire solar methanol fuel cell system, the incoming solar radiation, the molar inlet flow rate of methanol–water mixture, the length of the steam reformer, the length of the fuel cell, the inlet gas temperature of the fuel cell, the fuel-to-air ratio of the fuel cell, and the cell voltage of the fuel cell are chosen as input parameters to the numerical simulation.

The most characteristic result of the reformer is the methanol conversion efficiency or reformer efficiency,

$$\eta_{ref} = \frac{n'_{CH_3OH,in} - n'_{CH_3OH,out}}{n'_{CH_3OH,in}}, \tag{19}$$

indicating the ratio of converted methanol and methanol input. An important performance parameter of the fuel cell is the utilization factor of H_2,

$$U = \frac{n'_{H_2,in} - n'_{H_2,out}}{n'_{H_2,in}}, \tag{20}$$

calculated as the fraction of H_2 that is converted in the fuel cell. Finally, an essential parameter of this study is the total exergetic efficiency μ_{tot} of the entire fuel cell powerplant, defined as the ratio between the exergy output (i.e., the generated electric power P') and the exergy input (i.e., the exergy input of the solar radiation and the flow availability or exergy of methanol, water, and air at the inlets), given as

$$\mu_{tot} = \frac{P'}{a'_{solar} + a'_{CH_3OH,in} + a'_{H_2O,in} + a'_{air,in}}, \tag{21}$$

where the consumption of electrical power for the required pumping of the methanol–water mixture and the air flow through the system is neglected. The flow availabilities a'_j are defined as

$$a'_j = [h'_j(T) - h'_j(T_0)] - T_0[s'_j(T) - s'_j(T_0)] + n'_j \cdot RT_0 \cdot \ln(X_j) + a'_{chem,j}. \tag{22}$$

The index j refers to the chemical species with the mole fraction X_j. The entropy s_j is calculated with the same polynomial parameters used for the enthalpy h_j as defined by Eq. (5). The chemical availability $a'_{chem,j}$ is given by the reference environment model II of Table A-26 in [27]. The solar exergy input can be calculated by

$$a'_{solar} = I'_{solar,\,absorb} \cdot \left(\frac{1 - T_0}{T_{solar}}\right), \tag{23}$$

according to Press [34] and Edgerton [35], where T_0 is the ambient temperature (=298 K) and T_{solar} is the black-body solar temperature (=5775 K). Since the solar radiation can be seen as a 'cost-free' energy and exergy input, it is reasonable to define as well an exergetic efficiency only considering the conversion of exergy in form of (chemical) flow availability to electric power and neglect the solar exergy input:

$$\mu = \frac{P'}{a'_{CH_3OH,in} + a'_{H_2O,in} + a'_{air,in}}. \tag{24}$$

Beside the exergetic efficiency, an important criterion is the power density per area. Assuming that the area where the solar methanol fuel cell system can be installed is limited, it is interesting to know how much electric power can be generated per area that has to be exposed to solar radiation. The resulting solar power density P''_{solar}

$$P''_{solar} = \frac{P'}{L_{solar}} \tag{25}$$

can be used to compare the performance of the system with other area-based energy conversion techniques, especially with photovoltaic cells.

3. Results

3.1. Reference case

As the reference case, the mean terrestrial solar heat flux ($I_{solar} = 1000\ \text{W m}^{-2}$ integrated over the entire solar spectrum, equivalent to 1 sun for airmass 1.5) is assumed and the system is fed with a $2 \times 10^{-4}\ \text{mol m}^{-1}\ \text{s}^{-1}$ methanol–water mixture as liquid molar inlet flow rate per width. The steam reformer length is set to 10 mm and the fuel cell is 200 mm long. The fuel cell inlet temperature is 353 K (equal to the PROX outlet temperature), the stoichiometric oxygen-to-hydrogen ratio λ_{PEM} is 1, and the operating cell voltage E is 0.75 V.

These values result in a length of the methanol–water evaporator of 32.9 mm and of the air pre-heater of 2.9 mm, leading to a length of the entire solar module of 45.8 mm. The reforming efficiency η_{ref} amounts to 93.5%, the reformate gas contains $2.79 \times 10^{-4}\ \text{mol m}^{-1}\ \text{s}^{-1}$ H_2, and the CO mole fraction after the reformer is 0.53%. The glass layer on top of the solar module reaches a temperature of 326.6 K, while the inner silicon layers are heated to 589.5 and 589.0 K, respectively, and the bottom silicon layer is at 303.7 K. The maximum temperature of the fluid flow in the

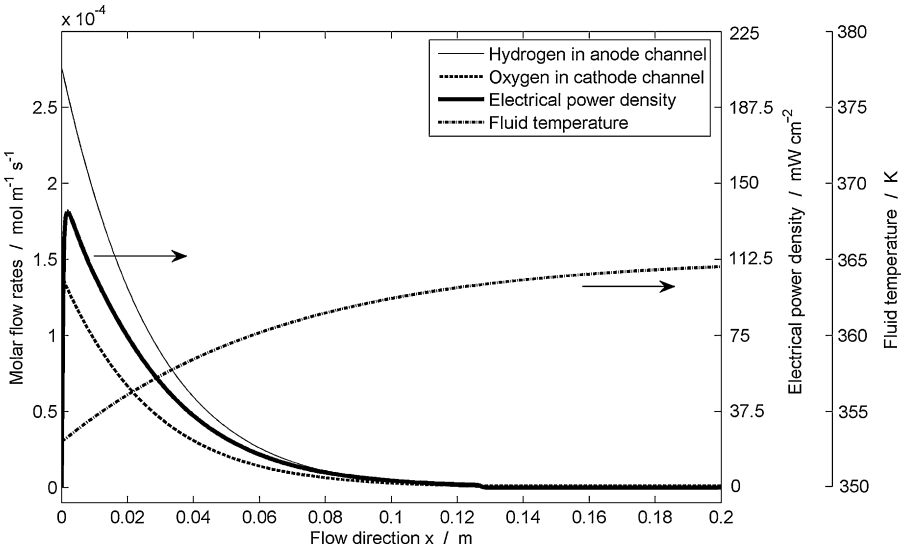

Fig. 3. Molar flow rates of hydrogen in the anode channel, oxygen in the cathode, electrical power density, and fluid temperature of the PEM fuel cell along the flow direction.

reformer is 589.1 K, basically identical with the surrounding wafers. The largest part of the solar module is required to evaporate the methanol–water mixture. The intermediate module is only 2.6 mm long and removes effectively most of the produced CO: the CO mole fraction after the PROX is 9.7 ppm and the gas mixture still contains 2.76×10^{-4} mol m^{-1} s^{-1} H_2, indicating only little H_2 oxidation in the PROX. The silicon layers of the intermediate module reach a temperature of 352.0 K, close to the operating temperature of the PROX reactor at 353 K.

The fuel cell generates 40.0 W m^{-1} electrical power output per width while converting practically 100% of the H_2. The outer surface of the silica aerogel insulation reaches a temperature of 304.6 K, whereas the inner silicon layers are a 365.1 K. The fluid flow heats up along the fuel cell from an inlet temperature of 353 K to the outlet temperature of 364.5 K, as shown in Fig. 3 next to the local molar flow rates of hydrogen in the anode channel, oxygen in the cathode and the electrical power density along the fuel cell. The exhaust gas contains traces of unconverted species with the following gas mole fractions: 0.7% methanol, 4.2 ppm CO, and below 1 ppm H_2.

The operating and geometrical conditions of the reference case lead to an electrical power output per width of 40.0 W m^{-1} and, with a total system length of 248.4 mm, to an electrical power density per solar area of 873 W m^{-2}. The solar module is irradiated with 45.8 W m^{-1}, where 40.2 W m^{-1} are effectively absorbed by the absorber coating and the remaining 5.6 W m^{-1} are directly reflected back to the ambient. All three modules release heat to the ambient by convection and radiation due to the temperature difference between the system and the ambient: 25.3 W m^{-1} by the solar module, 4.8 W m^{-1} by the intermediate module, and 26.3 W m^{-1} by the fuel cell.

The system has two different exergy inputs: the incoming solar heat flux accounts for an exergy input a'_{solar} of 43.4 W m^{-1} (where 38.1 W m^{-1} are effectively absorbed by the system and 5.3 W m^{-1} are directly reflected back to the ambient), and the flow availability of the inlet flows of air, water, and mainly methanol is 71.6 W m^{-1}. The exhaust gas still transfers a flow availability of 7.7 W m^{-1}, an exergy loss of 3.2 W m^{-1} is attributed to the heat losses, and the exergy destruction due to irreversible processes in the system account for 58.9 W m^{-1}. This results in a total exergetic efficiency μ_{tot} of 34.7%. However, if the 'cost-free' solar radiation is neglected, the effective exergetic efficiency μ amounts to an impressive value of 55.8%. The entire exergy flow through the system is shown in Fig. 4.

3.2. Effect of the fuel cell size

In the reference case, the molar inlet flow rate, the length of the reformer, and the length of the fuel cell were defined as the main parameters. To investigate the correlation between the size of the system (reformer and fuel cell length) and the molar inlet flow rate (of fuel), the length of the reformer has been kept constant at 1 cm and the length of the fuel cell as well as the inlet flow rate have been varied to find the optimal operating point.

In Fig. 5, the influence of the inlet flow rate on the reforming efficiency is shown for the constant reformer length of 1 cm. Clearly,

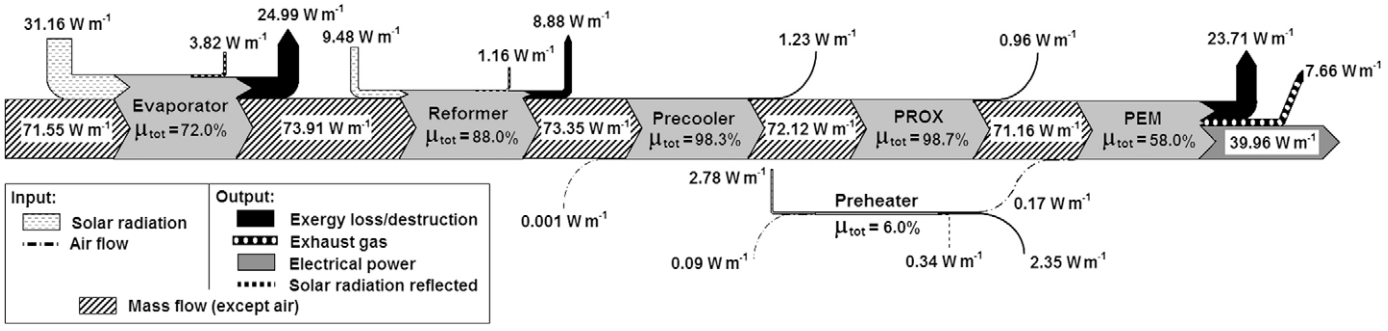

Fig. 4. Exergy flow through the entire solar-powered fuel cell system.

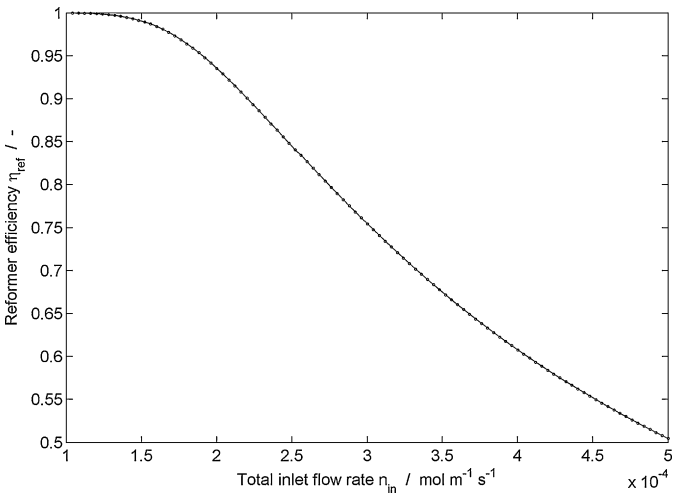

Fig. 5. Reforming efficiency as a function of the total inlet flow rate.

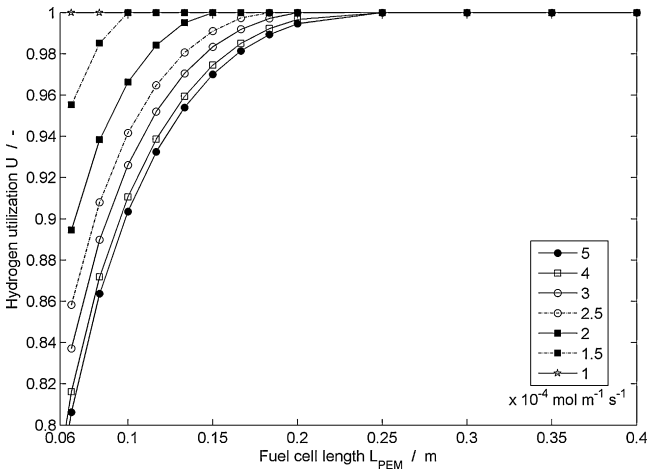

Fig. 7. Hydrogen utilization in the fuel cell as a function of inlet molar flow rate and fuel cell length.

the reforming efficiency drops with increasing inlet flow rate since the reformer is not long enough to reform all the methanol. Below 1.25×10^{-4} mol m^{-1} s^{-1}, 100% of the methanol is reacted, while at 2×10^{-4} mol m^{-1} s^{-1} (reference case) still about 93.5% conversion is achieved. For higher flow rates the reforming efficiency drops drastically.

In Fig. 6, the effect of the inlet flow rate and the fuel cell length on the electrical power output per width is shown. For shorter fuel cells (up to 0.2 m fuel cell length), the power output is low due to incomplete hydrogen utilization (as shown in Fig. 7). This simply means that the fuel cell is too short to convert all the produced hydrogen. For longer fuel cells, the power output is practically constant. The power output increases with an increasing inlet flow rate, however, this increase is rather small for high flow rates above 3×10^{-4} mol m^{-1} s^{-1}.

This effect can be seen even better if the exergetic efficiency (only accounting for the exergy input of the inlet flow and neglecting the 'cost-free' exergy input of the solar radiation) is considered (see Fig. 8). Although more electrical power can be generated for higher inlet flow rates, the exergetic efficiency drops remarkably for the higher inlet flow rates above 1.5×10^{-4} mol m^{-1} s^{-1}. Interestingly, a maximum in the exergetic efficiency can be found as a function of the inlet flow rate: for flow rates below 2×10^{-4} mol m^{-1} s^{-1} and the constant reformer length of 1 cm, the exergetic efficiency also drops. It exhibits a non-monotonic behavior leading to an optimal exergetic efficiency in the range between 1×10^{-4} and 2×10^{-4} mol m^{-1} s^{-1} of $\mu = 58.3\%$. This can be explained by an effect not shown by the reforming efficiency itself: The lower the inlet flow rate, the more methanol can be converted to hydrogen by steam reforming, but at the same time, the more carbon monoxide is produced in the reformer by undesired methanol decomposition. Therefore, if the reformer is too long for a certain inlet flow rate, more carbon monoxide has to be removed by the PROX reactor, causing an increased loss of hydrogen by this oxidation reaction. Although the reforming efficiency itself is increased for lower inlet flow rates and a constant reformer length, this does not necessarily increase the overall exergetic efficiency.

In addition to the electrical power output of the fuel cell and the exergetic efficiency, the power density per solar area is an important characteristic of the system, shown in Fig. 9. If the hydrogen utilization is 100%, the maximum solar power density for a specific inlet molar flow rate is reached, e.g. for fuel cell lengths longer than 0.2 m and inlet molar flow rates higher than 2×10^{-4} mol m^{-1} s^{-1}. The power density per solar area increases for a higher flow rate (up to 920 W m^{-2} for 2.5×10^{-4} mol m^{-1} s^{-1}) due to the increase in electrical power output, however, decreases for further increased flow rates due to the disproportionately higher length of the solar

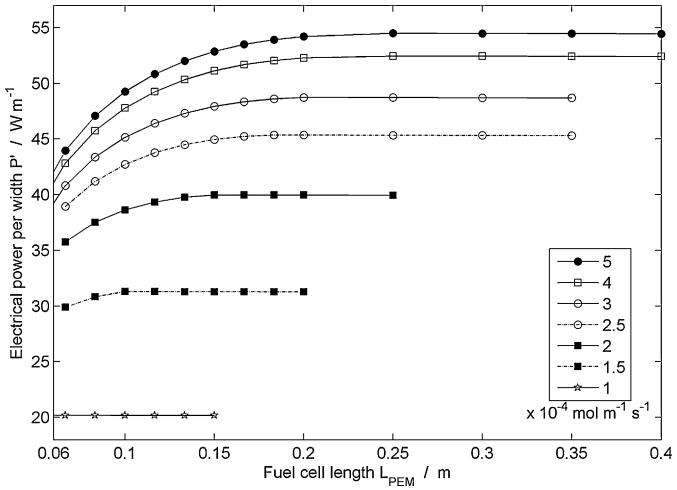

Fig. 6. Electrical power output per width as a function of inlet molar flow rate and fuel cell length.

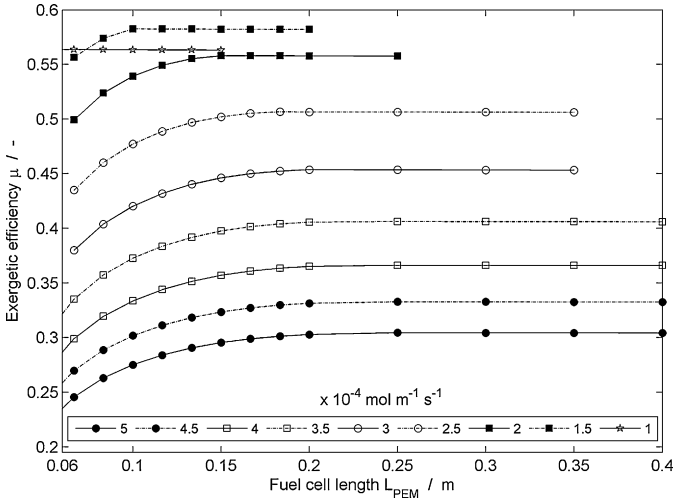

Fig. 8. Exergetic efficiency (only accounting for exergy input in form of inlet flow and neglecting 'cost-free' exergy input in form of solar radiation) as a function of inlet molar flow rate and fuel cell length.

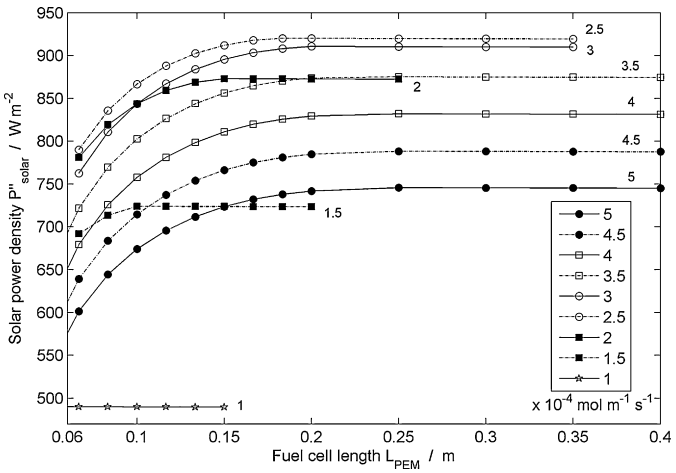

Fig. 9. Solar power density as a function of the inlet molar flow rate and the fuel cell length.

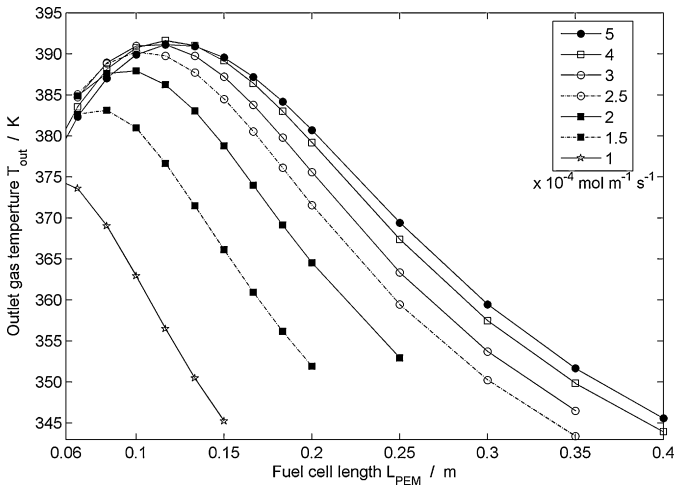

Fig. 10. Outlet gas temperature of the fuel cell as a function of the inlet molar flow rate and the fuel cell length.

module. Particularly the evaporation of the methanol–water mixture requires a large area irradiated by solar light for flow rates above 3×10^{-4} mol m^{-1} s^{-1}. For all tested inlet flow rates, a fuel cell length above 0.2 m has no effect on the solar power density. Nevertheless, increasing the fuel cell length has a positive and often essential effect: Since the area of the fuel cell is increased, more heat can be released to the ambient and the fuel cell temperature can be kept at a reasonable level.

This is better described by Fig. 10, in this case showing the temperature of the fuel cell exhaust gas as a characteristic temperature. For higher inlet flow rates, complete hydrogen utilization, and lower fuel cell lengths, insufficient heat is released from the fuel cell to the ambient and its temperature rises.

3.3. Effect of air-to-fuel ratio and cell voltage

Besides the essential question of an optimal correlation between system size and inlet flow rates, other operating parameters may have a significant effect on the efficiency and power output as well. As two examples, the air-to-fuel ratio of the fuel cell and the cell voltage are investigated.

In Fig. 11, the electrical power output and the exergetic efficiency are shown as functions of the cell voltage. It is clear that the cell voltage has an important effect on the performance of the fuel cell. Assuming that the cell voltage can be arbitrarily changed by the load, the efficiency can be further optimized by choosing an optimal cell voltage. For lower cell voltages, the fuel cell is not able to perform efficiently and for cell voltages below 0.62 V, the fuel cell is operated in the mass transfer limited regime, as it can be seen from the maximum local current density i_{max} in the fuel cell. For cell voltages above 0.8 V, the fuel cell can only convert limited amounts of H_2 to achieve these high voltages, leading to a drastic loss in hydrogen utilization U, electrical power output P' and exergetic efficiency μ. By only changing the cell voltage from 0.75 (reference case) to 0.785 V, the electrical power output is increased to 41.5 W m^{-1}, the solar power density to 906 W m^{-2} (not shown), and the exergetic efficiency to 57.9%.

In contrast to the cell voltage, the fuel-to-air ratio has only a very little effect on the overall performance of the system (not shown in detail). By increasing the inlet air flow rate to the fuel cell by a factor of 3, the fuel cell temperature can be slightly reduced, but the electrical power output remains basically unchanged.

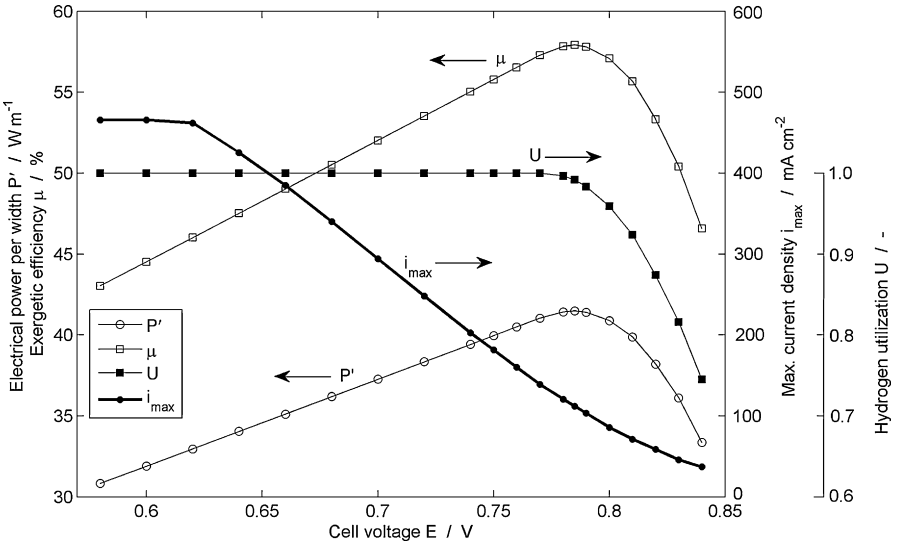

Fig. 11. Electrical power output per width, exergetic efficiency, maximum current density, and hydrogen utilization as functions of cell voltage.

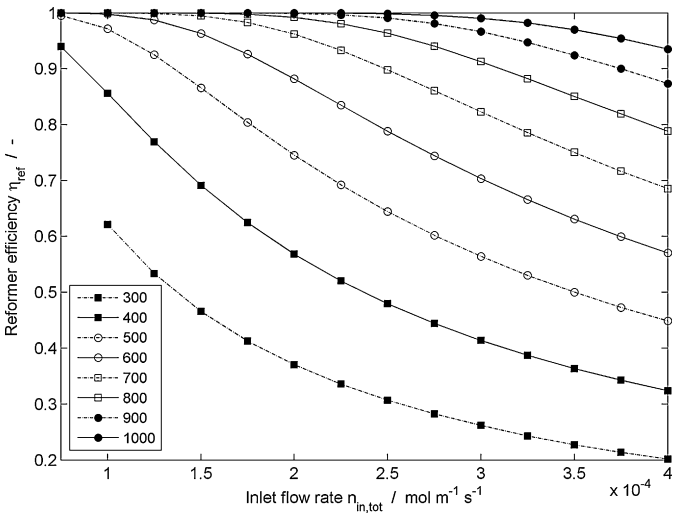

Fig. 12. Reformer efficiency as a function of total inlet flow rate and solar heat flux.

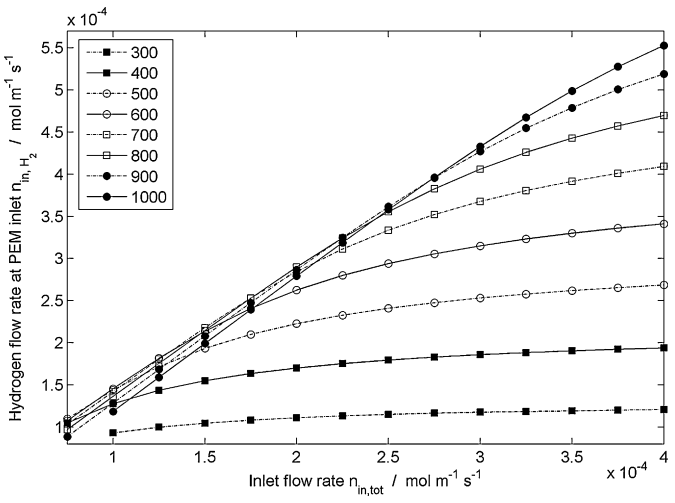

Fig. 13. Hydrogen flow rate at the fuel cell anode inlet as a function of total inlet flow rate and solar heat flux.

3.4. Effect of the intensity of solar radiation

The previous results are obtained under the assumption of a solar irradiance I_{solar} of 1000 W m^{-2}, indicating the input of solar energy integrated over the entire solar spectrum. To investigate the effect of non-optimal solar radiation, the system performance is analyzed for solar heat fluxes from 300 to 1000 W m^{-2}. The total inlet flow rate is varied from 0.75×10^{-4} to 4×10^{-4} mol m^{-1} s^{-1}, the reformer length is L_{ref} = 2 cm, and the fuel cell length is kept constant at L_{PEM} = 10 cm in contrast to the reference case. The change in reformer and fuel cell length is necessary to allow efficient steam reforming and a reasonable fuel cell temperature for the entire range of tested inlet flow rates and solar heat fluxes.

As shown in Fig. 12, the inlet flow rate has to be reduced significantly if the solar heat flux is reduced and the same reformer efficiency has to be kept constant: For I_{solar} = 900 W m^{-2}, the molar inlet flow rate has to be below 3.75×10^{-4} mol m^{-1} s^{-1} to achieve more than 90% reformer efficiency. This critical inlet flow rate drops to 2.5×10^{-4} mol m^{-1} s^{-1} for I_{solar} = 700 W m^{-2}, and 1.4×10^{-4} mol m^{-1} s^{-1} for I_{solar} = 500 W m^{-2}. For a solar heat flux below 300 W m^{-2}, the reformer can only be operated efficiently for a marginal inlet flow rate, since this solar heat flux cannot obtain the necessary minimum reformer temperature of 500 K. For high solar radiation and lower flow rates, the reformer reaches temperatures above 600 K, leading to the high methanol conversion rates presented in Fig. 12.

The positive effect on the H_2 production in the reformer by an increased reactor temperature is reduced by the inherently higher production of CO, especially above 600 K. The subsequent oxidation of CO in the PROX reactor reduces as well the effective amount of H_2 reaching the fuel cell, as shown in Fig. 13. For the solar irradiance increasing from 300 to 1000 W m^{-2}, the effective amount of H_2 increases for higher flow rates. However, for lower inlet flow rates, the effective H_2 flow rate to the fuel cell is higher for a lower solar heat flux. For example, more H_2 is produced for a solar heat flux of 800 W m^{-2} than for 1000 W m^{-2} if the inlet flow rate is below 2.5×10^{-4} mol m^{-1} s^{-1}. For 1.0×10^{-4} mol m^{-1} s^{-1}, the effective amount of hydrogen is higher for I_{solar} = 400 W m^{-2} than for 1000 W m^{-2}.

For the total inlet flow rates above 2×10^{-4} mol m^{-1} s^{-1}, the hydrogen utilization in the fuel cell drops below 100%, since the fuel cell is not long enough to convert all hydrogen. The higher the solar heat flux (and therefore, the higher the produced amount of hydrogen), the lower the hydrogen utilization of increased inlet flow rates. This leads to an alleviated increase in electrical power output with increasing inlet flow rates, especially for higher solar heat fluxes, as shown in Fig. 14. For the highest solar radiation, above 55 W m^{-1} can be achieved for a wide range of inlet flow rates. For a solar heat flux of 700 W m^{-2}, above 50 W m^{-1} electrical power can be generated, more than 35 W m^{-1} for 500 W m^{-2} of sunlight, and 16 W m^{-1} electrical power for 300 W m^{-2}.

The highest power density related to the solar area is achieved within the tested range of operating conditions for a solar heat flux of 1000 W m^{-2}, amounting to 679 W m^{-2} (Fig. 15). The peak power density decreases for lower radiation, however, still 305 W m^{-2} can be obtained for 500 W m^{-2}. The low solar flux of 300 W m^{-2} results in a solar power density of 115 W m^{-2}.

Interestingly, the maximum exergetic efficiency accounting only for the exergy input in form of inlet flow, as shown in Fig. 16, is relatively independent of the solar radiation. The maximum exergetic efficiency varies very slightly from 55.7% (for 1000 W m^{-2}) to 58.6% (for 700 W m^{-2}) and 59.0% (for 500 W m^{-2}). Nevertheless, the optimal inlet flow rate to reach maximal efficiency decreases with lower solar radiation and the maximum is not reached within the tested operating conditions for solar heat fluxes below 500 W m^{-2}.

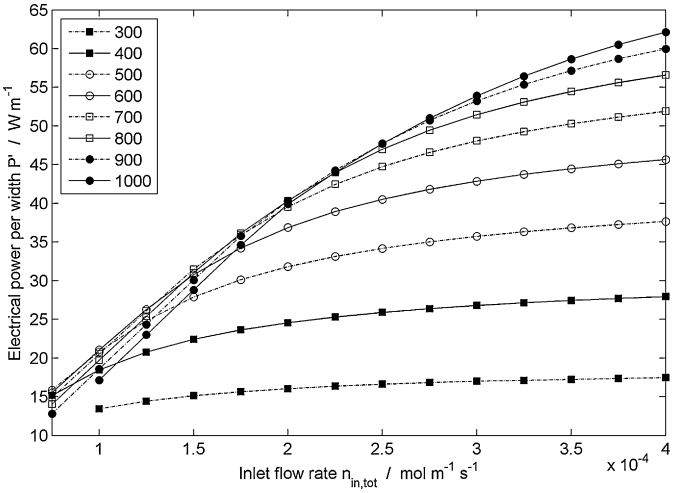

Fig. 14. Electrical power per width as a function of total inlet flow rate and solar heat flux.

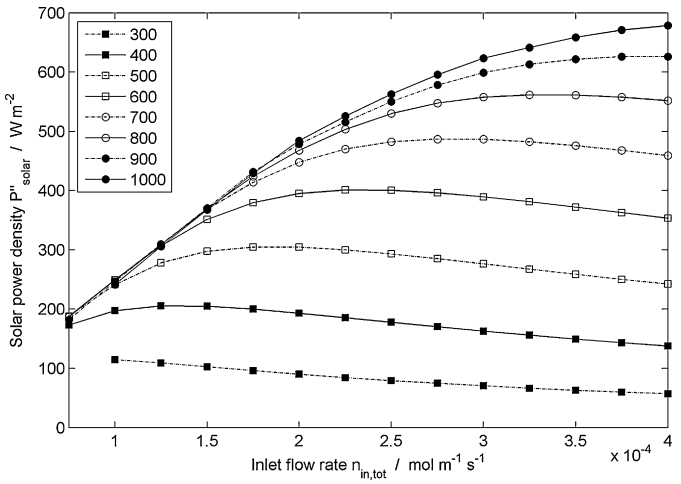

Fig. 15. Solar power density as a function of total inlet flow rate and solar radiation.

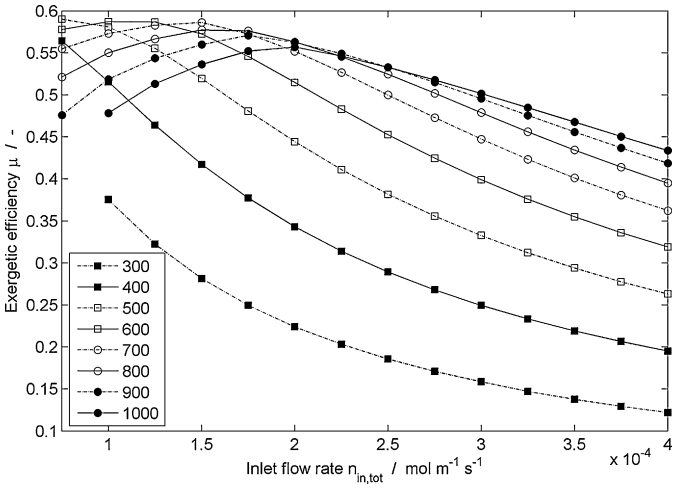

Fig. 16. Exergetic efficiency (only accounting for exergy input in form of inlet flow and neglecting 'cost-free' exergy input in form of solar radiation) as a function of total inlet flow rate and solar heat flux.

4. Discussion

4.1. Reference case

The results of the reference case clearly show that the proposed solar methanol fuel cell system can be operated very successfully and efficiently. For a solar irradiance of 1000 W m^{-2}, a reformer length of 10 mm, a fuel cell of 200 mm length, and a total system length of 248.4 mm are sufficient to achieve almost 94% methanol conversion, complete hydrogen utilization in the fuel cell, and a resulting generation of electrical power per width of 40.0 W m^{-1}. This leads to a total exergetic efficiency μ_{tot} of 34.7% and, if the 'cost-free' solar radiation is neglected for the exergy analysis, an impressive effective exergetic efficiency μ of 55.8%. This implies that the cost-effective exergetic efficiency can be increased by significantly more than half of its value by using solar radiation as a heat source instead of any other source (e.g. by burning a hydrocarbon or alcoholic fuel). The effective exergetic efficiency for the herein presented solar-powered system is significantly higher than any non-solar fuel cell system fed by hydrocarbon or alcoholic fuels. Compared with direct electricity production by photovoltaics, this is a very promising result since no currently commercially available solar cell can achieve such high power densities. A value of 873 W m^{-2} indicates an efficiency above 87% for equivalent photovoltaic systems which is not achievable with conventional photovoltaic cells. The best laboratory-scale photovoltaic cells currently reach sunlight-to-electricity efficiencies of about 40% [36–38], while commercially available cells are still very far away from this value. Therefore, the combination of exergy input in form of chemical fuel and solar radiation can be promising to achieve both a high exergetic efficiency and a high power density per area irradiated by sunlight.

4.2. Effect of the inlet flow rate, the fuel cell length, and the cell voltage

The electrical power is increased to more than 54 W m^{-1} for the highest inlet flow rate and adequate fuel cell length without increasing the exergetic efficiency. The fuel cell length has to be above 0.1–0.2 m depending on the flow rate to assure complete H_2 utilization. The positive effect of a decreased inlet flow rate on the production of H_2 is derogated by the simultaneously higher CO production in the reformer. For inlet flow rates below 2×10^{-4} mol m^{-1} s^{-1}, this has a seriously negative effect on the exergetic efficiency.

By decreasing the fuel cell length, the total area-specific power density of the system is increased simply because the total system length is decreased, as long as the H_2 utilization is kept high enough. However, the shorter fuel cell cannot release enough heat to the ambient and, therefore, this higher power density is achieved at the expense of higher fuel cell temperatures. If the temperature limit of 373 K has to be obeyed to achieve reliable and safe operating conditions, the reference case presents a good compromise between high power output, high exergetic efficiency, and high power density. The electrical power output could be increased by higher inlet flow rates, but this would decrease the exergetic efficiency and lead to too high fuel cell temperatures. Similarly, by decreasing the fuel cell length, the total power density could be significantly increased, but the fuel cell temperatures would increase significantly and at a certain point, the exergetic efficiency would drop as well.

The increase in fuel cell temperature causes two problems: First, the used numerical fuel cell model was designed for conventional PEM fuel cells operating approximately between 343 and 373 K (60–100 °C). Therefore, the results for higher inlet flow rates and a fuel cell length below 0.2 m will not be accurate anymore since the temperature is slightly outside the range of the model (up to 390 K). More importantly, because it is a practical problem, is the fact that (relatively cheap) PEM membranes can only be operated up to approximately 373 K since the membrane has to be hydrated by liquid water. Temperatures above 373 K are contradictory to cheap, commercially available PEM membranes for the current state of art of low-temperature fuel cells.

The proper choice of the cell voltage can increase the exergetic efficiency to 58% and the solar power density to 906 W m^{-2} by changing the cell voltage from 0.75 (reference case) to 0.785 V while obeying the restriction of an upper fuel cell temperature of 373 K. If the fuel cell is operated at reference conditions outside of the optimal cell voltage range between 0.75 and 0.8 V, the performance of the entire system drops significantly.

4.3. Effect of intensity of solar radiation

If the solar heat flux is below the maximum of 1000 W m^{-2} (equivalent to 1 sun for airmass 1.5), e.g. due to latitude, clouds, time of the day, or season, a constant reformer length requires lower inlet flow rates to achieve satisfactory reforming efficiency. This is caused by a lower reformer temperature that has to be above 500 K, preferably 550 K, for efficient system performance. Nevertheless, if the reformer temperature is too high, typically above

600 K, the enhanced production of CO leads to reduced electrical power generation.

Analogously to the H_2 production, the electrical power generated per system width is lower for reduced solar radiation, but even at a low 300 W m^{-2}, significant electrical power generation can be achieved. The power density per solar area is high as well for a solar heat flux 1000 W m^{-2} reaching a value of 679 W m^{-2}, indicating that a comparable photovoltaic system would need a sunlight-to-electricity efficiency above 67% to compete with the area-wise power density of our solar-powered fuel cell system. Even for lower radiation values, the solar power density reaches remarkably high values: a photovoltaic cell would be required to achieve a sunlight-to-electricity efficiency of 70% for a solar heat flux of 700 W m^{-2}, 61% for 500 W m^{-2}, and still 38% for the low radiation of 300 W m^{-2}. Such high efficiencies are beyond the theoretical limit of traditional photovoltaic systems and current maximum efficiencies are around 40% for expensive multi-junction concentrator cells under optimal conditions, as presented by Refs. [36–38].

These results show that the solar-powered fuel cell powerplant fed by methanol can be operated with very high efficiencies and power densities at a reduced intensity of solar radiation (even as low as 300 W m^{-2}), although the absolute amount of generated electrical power is significantly reduced for lower radiation. The exergetic efficiency is practically independent of the intensity of solar radiation at around 58%.

5. Conclusion

The results of the exergetic analysis prove that the proposed solar methanol fuel cell system can be operated very successfully and efficiently by combining methanol steam reforming and a PEM fuel cell with solar-powered heating. The cost-effective exergetic efficiency can be increased by a factor of around 1.6 (e.g. from 35% to 56% for the reference case) by using solar radiation as a heat source instead of any other source (e.g. by burning a chemical fuel), assuming that the exergetic efficiency of this alternative heating is as high as in the case of solar heating (around 88% of the exergy of the incoming solar heat flux are absorbed). The effective exergetic efficiency for the herein presented solar-powered system is significantly higher than any non-solar fuel cell system fed by hydrocarbon or alcoholic fuels.

By a proper choice of the operational and geometrical parameters, the exergetic efficiency accounting only for the chemical exergy input increases to 59% and the power density per solar area to 920 W m^{-2} for a maximum solar heat flux of 1000 W m^{-2}. Comparable photovoltaic systems would need excessive sunlight-to-electricity efficiencies of more than 92%. Therefore, the combination of exergy input in form of chemical fuel and solar radiation can be promising to achieve both, a high exergetic efficiency and a high power density per area irradiated by sunlight. Even for decreased intensities of solar radiation as low as 300 W m^{-2}, the system achieves very satisfactory results regarding solar power density and exergetic efficiency.

Acknowledgement

This work was partially supported by a scholarship of the Swiss National Science Foundation (SNSF) for N. Hotz.

References

[1] I. Aartun, B. Silberova, H. Venvik, P. Pfeifer, O. Gorke, K. Schubert, A. Holmen, Catal. Today 105 (3–4) (2005) 469–478.
[2] A. Bieberle-Huetter, D. Beckel, A. Infortuna, U. Muecke, J. Rupp, L. Gauckler, S. Rey-Mermet, P. Muralt, N. Bieri, N. Hotz, M. Stutz, D. Poulikakos, P. Heeb, P. Mueller, A. Bernard, R. Gmuer, T. Hocker, J. Power Sources 177 (1) (2008) 123–130.
[3] A. Chaniotis, D. Poulikakos, J. Power Sources 142 (1–2) (2005) 184–193.
[4] D. Hickman, L. Schmidt, Science 259 (5093) (1993) 343–346.
[5] N. Hotz, M. Stutz, S. Loher, W. Stark, D. Poulikakos, Appl. Catal. B-Environ. 73 (3–4) (2007) 336–344.
[6] N. Laosiripojana, S. Assabumrungrat, J. Power Sources 158 (2) (2006) 1348–1357.
[7] B. Silberova, H. Venvik, J. Walmsley, A. Holmen, Catal. Today 100 (3–4) (2005) 457–462.
[8] J.C. Amphlett, K.A.M. Creber, J.M. Davis, R.F. Mann, B.A. Peppley, D.M. Stokes, Intern. J. Hydrogen Energy 19 (2) (1994) 131–137.
[9] A. Kundu, J. Jang, H. Lee, S. Kim, J. Gil, C. Jung, Y. Oh, J. Power Sources 162 (1) (2006) 572–578.
[10] M.T. Lee, R. Greif, C.P. Grigoropoulos, H.G. Park, F.K. Hsu, J. Power Sources 166 (1) (2007) 194–201.
[11] M.T. Lee, D.J. Hwang, R. Greif, C.P. Grigoropoulos, Intern. J. Hydrogen Energy 34 (4) (2009) 1835–1843.
[12] D. Liguras, K. Goundani, X. Verykios, J. Power Sources 130 (1–2) (2004) 30–37.
[13] A. Pattekar, M. Kothare, J. Power Sources 147 (1–2) (2005) 116–127.
[14] J.S. Suh, M.T. Lee, R. Greif, C.P. Grigoropoulos, J. Power Sources 173 (1) (2007) 458–466.
[15] N. Hotz, M.T. Lee, C.P. Grigoropoulos, S.M. Senn, D. Poulikakos, Intern. J. Heat Mass Transfer 49 (15–16) (2006) 2397–2411.
[16] R. Zimmerman, G. Morrison, O. The, G. Rosengarten, Proceedings of the SPIE—The International Society for Optical Engineering 6800(A-1-11), 2007, p. 68001.
[17] R. Zimmerman, G. Morrison, G. Rosengarten, Proceedings of ASME 2nd International Conference on Energy Sustainability, Jacksonville, Florida, USA, August 10–14, 2008.
[18] A. Yilanci, I. Dincer, H.K. Ozturk, Intern. J. Hydrogen Energy 33 (24) (2008) 7538–7552.
[19] M. Granovskii, I. Dincer, M.A. Rosen, J. Fuel Cell Sci. Technol. 5 (3) (2008) 031005.
[20] S. Obara, I. Tanno, Intern. J. Hydrogen Energy 33 (9) (2008) 2300–2310.
[21] V.M. Janardhanan, V. Heuveline, O. Deutschmann, J. Power Sources 172 (1) (2007) 296–307.
[22] N. Hotz, S. Senn, D. Poulikakos, J. Power Sources 158 (1) (2006) 333–347.
[23] H. Renon, C.A. Eckert, J.M. Prausnitz, Ind. Eng. Chem. Proc. Des. Dev. 7 (2) (1968) 220–225.
[24] H. Renon, C.A. Eckert, J.M. Prausnitz, Ind. Eng. Chem. Fundam. 6 (1) (1967) 52–58.
[25] H. Renon, J.M. Prausnitz, AIChE J. 14 (1) (1968) 135–144.
[26] S. Horstmann, P. Mougin, F. Lecomte, K. Fischer, J. Gmehling, J. Chem. Eng. Data 47 (6) (2002) 1496–1501.
[27] M.J. Moran, D.N. Shapiro, Fundamentals of Engineering Thermodynamics, 4th ed., Wiley, 1999.
[28] American Institute of Chemical Engineers/Design Institute for Physical Properties, DIPPR® project 801—evaluated standard thermophysical property values, full version, 2009.
[29] T.E. Springer, T. Rockward, T.A. Zawodzinski, S. Gottesfeld, J. Electrochem. Soc. 148 (1) (2001) A11–A23.
[30] S.H. Chan, S.K. Goh, S.P. Jiang, Electrochim. Acta 48 (13) (2003) 1905–1919.
[31] M.J. Kahlich, H.A. Gasteiger, R.J. Behm, J. Catal. 182 (2) (1999) 430–440.
[32] V. Gurau, F. Barbir, H.T. Liu, J. Electrochem. Soc. 147 (7) (2000) 2468–2477.
[33] T.E. Springer, T.A. Zawodzinski, S. Gottesfeld, J. Electrochem. Soc. 138 (8) (1991) 2334–2342.
[34] W.H. Press, Nature 264 (1976) 734–735.
[35] R.H. Edgerton, Energy 5 (1980) 693–707.
[36] R.R. King, D.C. Law, K.M. Edmondson, C.M. Fetzer, G.S. Kinsey, H. Yoon, R.A. Sherif, N.H. Karam, Appl. Phys. Lett. 90 (2007) 183516.
[37] J.F. Geisz, S. Kurtz, M.W. Wanlass, J.S. Ward, A. Duda, D.J. Friedman, J.M. Olson, W.E. McMahon, T.E. Moriarty, J.T. Kiehl, Appl. Phys. Lett. 91 (2) (2007), 23502/1-3.
[38] S. Kurtz, D. Myers, W.E. McMahon, J. Geisz, M. Steiner, Prog. Photovolt. 16 (6) (2008) 537–546.